Mon. Not. R. Astron. Soc. **000**, 1–16 (2014) Printed 24 February 2015 (MN LATEX style file v2.2)

How elevated is the dynamical-to-stellar mass ratio of the ultra-compact dwarf S999?

Joachim Janz[1⋆], Duncan A. Forbes[1], Mark A. Norris[2], Jay Strader[3], Samantha J. Penny[4,1,5], Martina Fagioli[1,6], Aaron J. Romanowsky[7,8]
[1] *Centre for Astrophysics & Supercomputing, Swinburne University, Hawthorn, VIC 3122, Australia*
[2] *Max Planck Institut für Astronomie, Königstuhl 17, D-69117, Heidelberg, Germany*
[3] *Department of Physics and Astronomy, Michigan State University, East Lansing, Michigan 48824, USA*
[4] *School of Physics, Monash University, Clayton, Victoria 3800, Australia*
[5] *Institute of Cosmology and Gravitation, University of Portsmouth, Dennis Sciama Building, Burnaby Road, Portsmouth, PO1 3FX, United Kingdom*
[6] *Institute for Astronomy, ETH Zürich, Wolfgang-Pauli-Str. 27, 8093 Zürich, Switzerland*
[7] *Department of Physics and Astronomy, San José State University, San Jose, CA 95192, USA*
[8] *University of California Observatories, 1156 High Street, Santa Cruz, CA 95064, USA*

Accepted 2014 –. Received 2014 –; in original form 2014 –

ABSTRACT

Here we present new Keck ESI high-resolution spectroscopy and deep archival *HST*/ACS imaging for S999, an ultra-compact dwarf in the vicinity of M87, which was claimed to have an extremely high dynamical-to-stellar mass ratio. Our data increase the total integration times by a factor of 5 and 60 for spectroscopy and imaging, respectively. This allows us to constrain the stellar population parameters for the first time (simple stellar population equivalent age = $7.6^{+2.0}_{-1.6}$ Gyr; $[Z/\mathrm{H}] = -0.95^{+0.12}_{-0.10}$; $[\alpha/\mathrm{Fe}] = 0.34^{+0.10}_{-0.12}$). Assuming a Kroupa stellar initial mass function, the stellar population parameters and luminosity ($M_{F814W} = -12.13 \pm 0.06$ mag) yield a stellar mass of $M_* = 3.9^{+0.9}_{-0.6} \times 10^6 M_\odot$, which we also find to be consistent with near-infrared data. Via mass modelling, with our new measurements of velocity dispersion ($\sigma_{ap} = 27 \pm 2$ km s^{-1}) and size ($R_e = 20.9 \pm 1.0$ pc), we obtain an elevated dynamical-to-stellar mass ratio $M_{dyn}/M_* = 8.2$ (with a range $5.6 \leqslant M_{dyn}/M_* \leqslant 11.2$). Furthermore, we analyse the surface brightness profile of S999, finding only a small excess of light in the outer parts with respect to the fitted Sérsic profile, and a positive colour gradient. Taken together these observations suggest that S999 is the remnant of a much larger galaxy that has been tidally stripped. If so, the observed elevated mass ratio may be caused by mechanisms related to the stripping process: the existence of an massive central black hole or internal kinematics that are out of equilibrium due to the stripping event. Given the observed dynamical-to-stellar mass ratio we suggest that S999 is an ideal candidate to search for the presence of an overly massive central black hole.

Key words: galaxies: star clusters; general – galaxies: clusters: individual: Virgo Cluster – galaxies: dwarf

1 INTRODUCTION

Ultra-compact dwarfs (UCDs) are a class of compact stellar system that was only discovered some 15 years ago (Hilker et al. 1999; Drinkwater et al. 2000). Their sizes ($10 \lesssim R_e \lesssim 100$ pc) and masses ($10^6 \lesssim M/M_\odot \lesssim 10^8$) are intermediate between those of globular clusters (GCs) and compact ellipticals (cEs). Initially, they were called 'galaxies' but today it is still debated whether UCDs are the high mass end of the globular cluster population (e.g. Mieske et al. 2002; Forbes et al. 2008), or are the surviving nuclei of galaxies that were torn apart by tidal forces (e.g. Bassino et al. 1994; Bekki et al. 2001; Pfeffer & Baumgardt 2013). There is now growing evidence that both of these formation channels contribute to the UCD population (e.g. Mieske et al. 2006; Brodie et al. 2011; Chilingarian et al. 2011; Norris & Kannappan 2011; Penny et al. 2012).

Recently Norris et al. (2014a) presented sizes, stellar masses and internal velocity dispersion measurements for a large sample of UCDs. Velocity dispersions, coupled with

⋆ E-mail: jjanz@swin.edu.au

size, provide an estimate of the dynamical mass that is relatively insensitive to the distribution of stellar orbits (Wolf et al. 2010). Early studies, based on smaller samples of UCDs, detected a trend for the dynamical mass-to-light ratio (or equivalently the dynamical-to-stellar mass ratio) to increase steadily with increasing stellar mass (Forbes et al. 2008; Dabringhausen et al. 2008; Mieske et al. 2008b). Using the largest sample to date of data from the literature, Forbes et al. (2014) showed that this trend persisted for the general population of UCDs even up to stellar masses of $\sim 10^9$ $M_\odot$.

Several (non-exclusive) explanations for these elevated mass ratios have been offered, including a non-canonical stellar initial mass function (IMF; both a bottom or top-heavy IMF would lead to an underestimation of the stellar mass; e.g. Mieske et al. 2008a; Dabringhausen et al. 2009, 2010, 2012), the presence of dark matter (e.g. Baumgardt & Mieske 2008; Mieske et al. 2008a) and a central massive black hole raising the velocity dispersion (Mieske et al. 2013). The latter possibility has been dramatically confirmed recently by Seth et al. (2014) who detected an oversized central black hole in M60-UCD1 (Strader et al. 2013) that represents 15 per cent of the mass of the object. Although, interestingly despite the presence of this massive black hole M60-UCD-1 does not display a strongly elevated mass ratio based on its unresolved velocity dispersion (e.g. Forbes et al. 2014 found a dynamical-to-stellar mass ratio of about unity).

Forbes et al. (2014) also noted half a dozen UCDs with extremely high mass ratios (i.e. up to 10). Such UCDs are of particular interest. They may represent a rare subpopulation of UCDs that have been caught in the early stages of the stripping process, having effectively inflated sizes (or even outer halo structures) relative to their stellar mass. This may be the case for VUCD7 which reveals a core and halo structure in its surface brightness profile (Evstigneeva et al. 2008). Using the size and stellar mass of the core gives a dynamical-to-stellar mass ratio that is $\sim 3\times$ lower (although still higher than the typical UCD). We also note the recent discovery of a halo around the Milky Way globular cluster NGC 1851 (Marino et al. 2014). The presence of this halo of extra tidal light suggests that NGC 1851 was once the nucleus a dwarf galaxy, which was tidally stripped as it interacted with the Milky Way.

However, another more mundane possibility is that some of the measurements in the literature for these extreme objects are spurious. This appears to be the case for M59cO which had a high mass ratio based on the measurement of Chilingarian & Mamon (2008) using a low resolution spectrum from the Sloan Digital Sky Survey. Obtaining a medium resolution spectrum from the Keck telescope yield a new velocity dispersion measurement, which Forbes et al. (2014) showed gives its re-calculated mass ratio to be within the scatter of the UCD population as a whole.

Haşegan et al. (2005) studied a small number of UCDs around M87. They calculated a dynamical mass-to-light ratio for half a dozen objects, finding one (called S999) to have the highest ratio of 9.36 ± 0.94.[1] In the list of over 50 UCDs by Mieske et al. (2008b), the UCD with the highest mass-to-light ratio was also S999 with $M/L_V = 10.2$. In the Forbes et al. (2014) study, it has a similarly extreme dynamical-to-stellar mass ratio. In both the Mieske et al. and Forbes et al. works the velocity dispersion, size and luminosity of S999 are based on the measurements of Haşegan et al. (2005).

As well as an extreme mass ratio, S999 also has a particularly low stellar mass and low density for a UCD. These extreme properties call for a confirmation of the mass ratio. Here we take advantage of a very deep ACS pointing from the *HST* in two filters, to remeasure the size and photometry of S999. In particular, we search for an extended halo in the surface brightness profile which may indicate ongoing stripping. We also present new high-quality Keck spectroscopy from which we obtain the velocity dispersion and stellar population properties (which in turn provide an improved estimate for the stellar mass). We also analyse the surface brightness profile of seven other UCDs around M87 (within the deep ACS field of view) to search for extended halo light.

Table 1. M87 UCDs in the field of view of the ACS observations

Name	Right Ascension (h:m:s)	Declination (d:m:s)	$V_{\rm hel}$ ($km\ s^{-1}$)
S999	12:30:45.91	+12:25:01.5	1466 ± 5
H44905	12:30:57.08	+12:23:39.8	1563 ± 18
S672	12:30:54.73	+12:21:38.3	735 ± 106
S887	12:30:48.93	+12:21:55.6	1811 ± 106
S928	12:30:47.70	+12 24 30.4	1283 ± 5
S5065	12:30:50.05	+12:24:08.9	1578 ± 3
S8005	12:30:46.20	+12:24:23.1	1883 ± 5
S8006	12:30:46.65	+12:24:22.2	1079 ± 5

The equinox of the coordinates is J2000. The data is taken from the compilation in Strader et al. (2011), following their naming scheme with the Hanes et al. (2001) extension of the Strom et al. (1981) nomenclature.

2 OBSERVATIONS AND DATA REDUCTION

This study is based on very deep archival *HST* images of S999 and seven more UCDs in the same field of view, and a newly obtained spectrum of S999 from the Keck telescope. In the following paragraphs the data acquisition and reduction are described. Here we assume that the UCDs are located at the same distance as M87, for which surface brightness fluctuations and the tip of the red giant branch give consistent values, i.e. 16.7 Mpc (Blakeslee et al. 2009; Bird et al. 2010; see also Brodie et al. 2014),[2] which means that one arcsecond corresponds to $1'' = 80.35$ pc.

[1] With the updated uncertainty of the velocity dispersion (see Section 3.3) the uncertainty of the dynamical mass becomes ± 1.97.

[2] In the literature often a distance of 16.5 Mpc was assumed for the M87 UCDs. Both the inferred physical size and stellar mass would be reduced by 1-3%. In the mass ratio this cancels partly, and the derived ratio for a distance of 16.5 Mpc would be larger by 1.2%.

2.1 *HST* ACS Imaging

Very deep archival *HST* Advanced Camera for Surveys (ACS) images are available in two filters (F606W and F814W, wide V and I, respectively) from the *HST* GO programme 10543 (PI Baltz). While the original purpose of the observations was to study microlensing towards M87, the images have also been used to study its globular cluster system (Waters et al. 2009; Peng et al. 2009; Madrid et al. 2009; Webb et al. 2012). Similarly, we used the depth and resolution of the observations to obtain surface brightness profiles of S999 and seven other UCDs within this field of view. Furthermore, we processed the overlapping ACS Virgo Cluster Survey pointings (ACS VCS, Côté et al. 2004) F475W (g) and F850LP (z) in the same fashion in order to enable a comparison of our measurements to the ACS VCS study of compact stellar systems (Haşegan et al. 2005).

The pipeline processed *FLT.fits* images were downloaded from the Mikulski Archive for Space Telescopes (MAST) archive[3] and further reduced with the latest *HST* ACS pipeline *astrodrizzle*, similar to Madrid et al. (2009). The observations were carried out with a dither pattern allowing for subpixel drizzling, so that the original pixel size of $0\farcs05$ was decreased to $0\farcs035$. The drizzled and shifted images were combined with the IRAF task `imcombine`, the magnitudes were calibrated to the Vega system using the provided zeropoints[4] and corrected for Galactic extinction according to Schlegel et al. (1998).[5]

The field of view is filled with the light from M87. In order to study the light distributions of the UCDs, especially at faint surface brightness levels in their outskirts, the light of M87 needed to be removed with high precision. This was achieved by first subtracting from each pixel the median value of those in a 101×101 pixel box around that pixel (see also Madrid et al. 2009). On this preliminarily processed image we ran SExtractor (Bertin & Arnouts 1996) to create an object mask. The final model of M87 was created by a combination of the IRAF tasks `ellipse` and `bmodel` using that object mask. The final model was subtracted from the image before any further analysis was carried out. We found a remaining non-zero local background around the UCDs. Therefore, we subtracted the average of the mean pixel values in the surrounding eight boxes of a 3×3 grid with a total width of 201 pixels centred on each UCD (see Fig. 1). The uncertainty of the background was estimated by the scatter of these values and the mean values of 16 further boxes, which were placed at distances to the centre of M87 similar to those of the UCDs. An image of S999 and a few globular clusters in the surroundings are shown in Fig. 1.

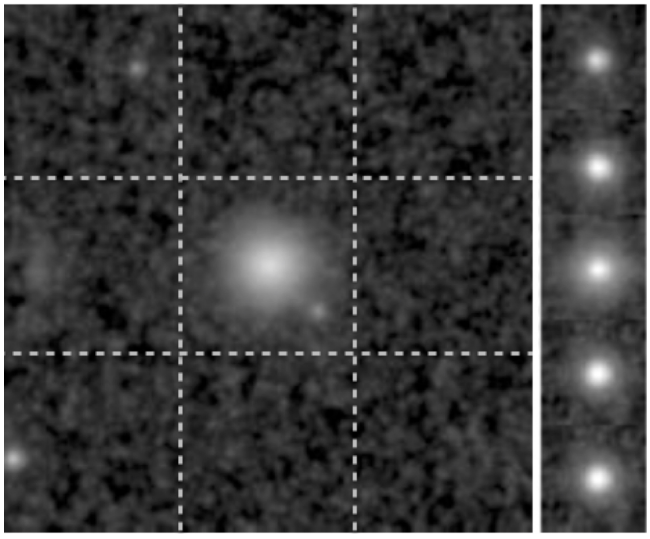

Figure 1. Image of S999. *Left* panel: $F814W$-band image of S999 with the light of M87 subtracted. The panel displays 201×201 pixels or $\sim 7'' \times 7''$; at the assumed distance of 16.7 Mpc, $1'' = 80.35$ pc. The grid indicates the eight surrounding boxes around S999 which were used to determine the local background values. *Right* panels: five globular clusters from Strader et al. (2011), which are close to S999 in projection, shown on the same pixel and grey scale for comparison.

2.1.1 *Surface brightness profiles*

The surface brightness profiles of S999 and seven more UCDs in the ACS field of view (Fig. 2 and A1) were measured with the `ellipse` task of IRAF (Jedrzejewski 1987). During the process fore- and background objects were masked. The position angle and ellipticity of the isophotes were fixed to values obtained by averaging the isophotes with semi-major axis lengths between $0\farcs25$ and $0\farcs6$ from a preliminary profile measurement (with the two quantities as free fitting parameters). The spatial range was chosen such that the measurements were unaffected by the point spread function (PSF) and benefited from a high signal-to-noise. The UCDs are all quite round (axis ratios b/a from 0.84 to 0.97). However, the isophotes in the outskirts can be severely biased by extreme pixel values due to noise in the images. The not well-constraint isophotes vary unreasonably to random values of position angle and ellipticities, and especially the latter biases the surface brightness profile. For our specific question – looking for signs of extended envelopes in the outer parts of the UCDs – this was much less acceptable than the potential loss of information from fixing position angle and ellipticity. The azimuthally averaged surface brightness profiles reach typically a surface brightness in the I-band of ~ 24 mag arcsec^{-2} at 3 to 5 half-light radii.

We fitted Sérsic profiles to the measured surface brightness profiles along the semi-major axes using a nonlinear least-squares Levenberg-Marquardt algorithm, weighting the individual measurements with the inverse squared of the uncertainties as provided by the ellipse task. For the fits we excluded the innermost $0\farcs15$ so as not to be affected by the PSF (the typical full-width at half maximum of the PSF for the ACS wide-field camera is $\sim 0\farcs1$).

2.1.2 *Photometry*

The photometry for the eight UCDs in the ACS field of view was obtained in two different ways: a non-parametric approach and via fitted Sérsic functions.

[3] `http://archive.stci.edu`
[4] `http://www.stsci.edu/hst/acs/analysis/zeropoints/zpt.py`
[5] The difference in the attenuation as compared to Schlafly & Finkbeiner (2011) is smaller than 0.015 mag in all bands.

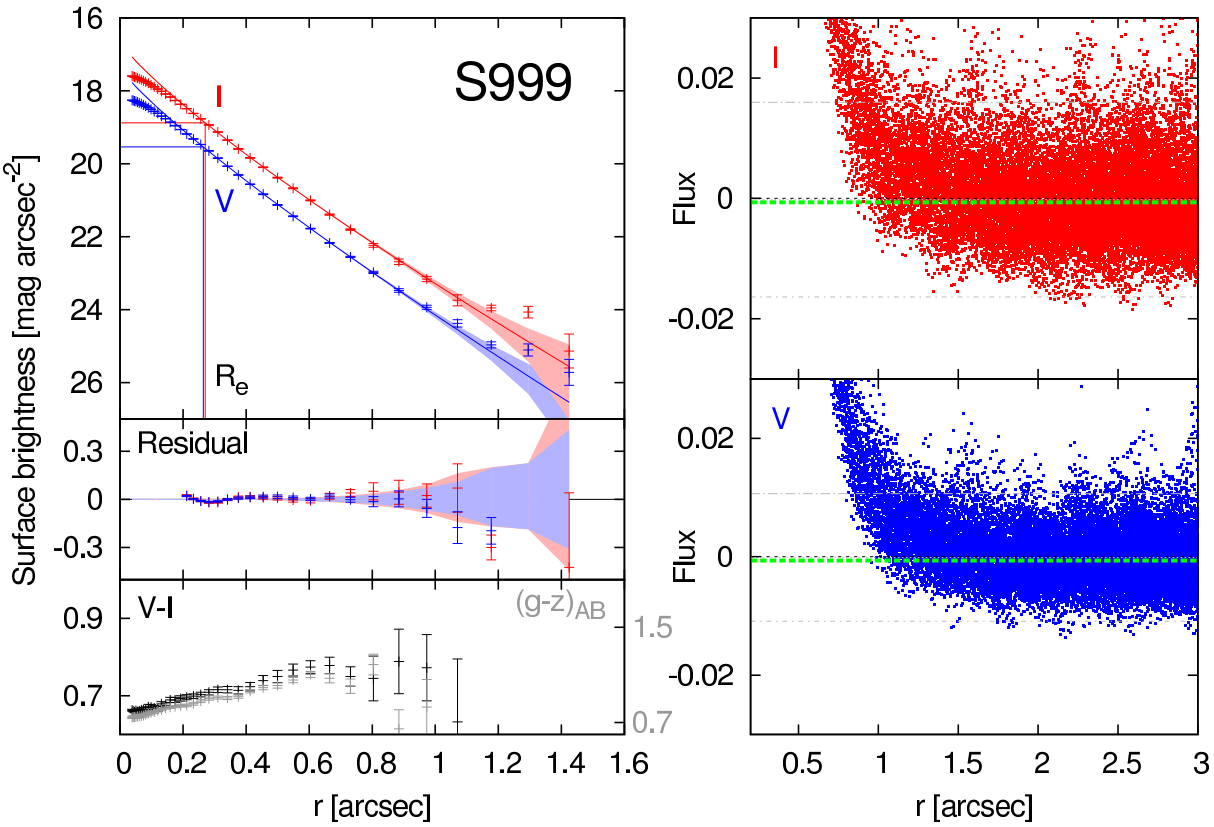

Figure 2. Surface brightness and colour profiles of S999. *Left:* from *top* to *bottom* are the surface brightness profiles and Sérsic fits, the residuals of the profile fits, and the F606W-F814W ($V-I$, black) and F475W-F850LP ($g-z$) colour profiles (grey, with scale on right side). Red and blue colours represent F814W and F606W, respectively. The shaded areas in the upper two panels display the systematic uncertainty of the background determination, while the error bars display the measurement uncertainty as given by the `ellipse` task of IRAF. The vertical and horizontal lines in the surface brightness profile panel indicate the half-light radius and the surface brightness at this radius (at the assumed distance of 16.7 Mpc, $1'' = 80.35$ pc). *Right:* Pixel values on a linear scale for F814W *(top)* and F606W *(bottom)* to assess the background subtraction, with the green horizontal line displaying the average pixel value at radii between $2''$ and $3''$ after a 2.3σ clipping.

For the non-parametric approach we followed Janz & Lisker (2008) and determined (elliptical) Petrosian apertures (Petrosian 1976). The total flux and half-light semi-major axis length a_e were then measured in an aperture with twice the Petrosian semi-major axis length, and corrected for the missing flux following the prescriptions of Graham et al. (2005). The parametric photometry was calculated from the Sérsic fits to the light profiles using the formulae provided in Graham & Driver (2005).

Our photometric measurements are summarised in Table 2. The deviations between non-parametric and parametric photometry can be attributed to effects of the PSF, as the two objects with the greatest difference are those with the largest Sérsic n, and hence the steepest profile in the innermost region. The uncertainty on the individual measurements is small, which can be seen by the consistency of the systematic increase of size with wavelength along the sequence *g*-*V*-*I*-*z* with the positive colour gradient of S999 (Tables 2 and A1). Furthermore, the $V-I$ colours inferred from the total magnitudes from the two methods of measuring photometry are consistent. Our measurements on the ACS VCS images are very consistent with those of Haşegan et al. (2005) using the same data: the typical deviation for the magnitudes and radii derived from the profile fits (Haşegan et al. used King profiles) for the three UCDs in common is at the 5% level. In the subsequent analysis we consider this as the uncertainty level for the luminosities and radii (see also Table 3), and adopt the average circularised radius from the two Sérsic fits as the size $R_e = 20.9$ pc.

2.2 Near-infrared photometry of S999

In addition we measured the K_s-band magnitude of S999 from archival WIRCam (Puget et al. 2004) imaging of M87 taken as part of the Next Generation Virgo Cluster Survey-IR (Muñoz et al. 2014). The final calibrated K_s-band stacked image of M87 was downloaded from the CADC archive, this had a total integration time of 4487s and provided image quality of 1.31 arcseconds; sufficient for the measurement of a total integrated magnitude of S999 but not for any examination of spatially resolved properties. The downloaded image was first analysed to remove the halo of M87 using the procedure described in Norris & Kannappan (2011). The total integrated K-band magnitude of S999 was then measured with SExtractor (Bertin & Arnouts 1996) yielding a magnitude of 17.71 ± 0.03 or $M_{K_s} = -13.40 \pm 0.03$ mag.

Table 2. Photometry of UCDs around M87

UCD	Non-parametric				Sérsic fit								b/a	PA
	F606W (V)		F814W (I)		F606W (V)				F814W (I)					
	m	a_e [$''$]	m	a_e [$''$]	m	a_e [$''$]	μ_e	n	m	a_e [$''$]	μ_e	n		[°]
S999	19.78	0.29	19.05	0.30	19.71	0.26	19.54	1.2	18.98	0.27	18.88	1.2	0.96	8.8
H44905	21.38	0.27	20.65	0.28	21.32	0.25	20.94	0.9	20.62	0.26	20.28	0.8	0.97	-53.1
S672	20.34	0.24	19.62	0.24	20.04	0.17	19.20	2.1	19.43	0.20	18.78	1.8	0.94	-30.0
S887	20.60	0.18	19.82	0.19	20.12	0.11	18.49	2.6	19.45	0.13	18.09	2.4	0.96	-54.6
S928	19.27	0.34	18.58	0.35	19.19	0.30	19.38	1.5	18.52	0.31	18.75	1.4	0.92	-6.7
S5065	19.67	0.21	18.93	0.22	19.45	0.17	18.43	1.2	18.74	0.18	17.81	1.2	0.97	27.9
S8005	19.96	0.39	19.25	0.39	19.94	0.36	20.31	1.2	19.26	0.36	19.62	1.2	0.84	16.6
S8006	20.02	0.28	19.32	0.28	19.91	0.24	19.64	1.3	19.19	0.24	18.90	1.3	0.96	16.4

The semi-major axis length a_e of the apertures containing half of the light is given in arcseconds and the surface brightness μ_e of the corresponding isophote in mag arcsec^{-2}; m is the total magnitude. The final two columns list the minor-to-major axis ratio (b/a) and position angle (PA) in degrees. At the assumed distance of 16.7 Mpc, one arcsecond corresponds to $1'' = 80.35$ pc. The photometry based on the ACS VCS pointing is summarised in Table A1.

2.3 Keck ESI Spectrum of S999

A high-quality spectrum for the UCD S999 was observed during the night of the 2014 March 21 with the Echelle Spectrograph and Imager (ESI, Sheinis et al. 2002) with the Keck II telescope with a total integration time of 3.2 hours, resulting in a signal-to-noise of $S/N \sim 20$ per Ångström. The centre of the UCD was placed in the middle of the slit, which was aligned with the parallactic angle (PA= $-73°$). In total seven exposures were obtained (one with an integration time of 600s and six with 1800s) in the echellette mode using a $0\farcs75 \times 20''$ slit, with the seeing varying between $0\farcs5$ and $0\farcs6$. The setup results in a resolving power of $R \sim 5400$. The ten Echelle orders span a wavelength range of approximately 3900 to 11000 Å. The spatial scale corresponds to $0\farcs12$ to $0\farcs17$ per pixel from the blue to red end of the spectrum.

From the several frames for each of the calibrations (internal flat fields, bias, arc lamps) we determined master calibration frames by combining the two-dimensional spectra using the `imcombine` task in IRAF. The individual science spectra were reduced with the pipeline MAKEE (T. Barlow). The software takes care of the flat fielding and bias subtraction. It also uses a spectrum of a star to trace the Echelle orders in order to extract a one-dimensional spectrum for each order, which is then wavelength calibrated using the known lines of the arc lamps (of a previous observing run using a similar setup). Also an error spectrum, i.e. the individual uncertainties of the pixels in the spectrum, is calculated.

The flat fielding does not bring the various Echelle orders to a common flux level. Therefore, we took the spectrum of a velocity standard (HR3454) observed with the same setup and obtained the blaze function by comparing that spectrum to a published spectrum of the same star (Le Borgne et al. 2003). The Echelle orders of the corrected spectrum overlap. The various exposures and different Echelle orders are finally combined to a single spectrum in a signal-to-noise optimised way using UVES_popler (M.T. Murphy). The uncertainties are propagated through the scaling and combination processes in order to obtain a final error spectrum.

The ESI spectrum of S999 was fitted with a penalised pixel fitting code, pPXF (Cappellari & Emsellem 2004), using stellar spectra of the ELODIE library (Prugniel & Soubiran 2001, version 3.1). The library contains spectra of 1388 stars, which cover a wavelength region of 3900 Å to 6800 Å at a resolution of $\sigma \sim$12 km s^{-1} (R$\sim$10,000), and which span a wide range of spectral type and metallicity. For the fitting, the template stars were convolved to the instrumental resolution (with a constant $\sigma = 21$ km s^{-1}), taking into account the templates' resolution. The spectral range used for the fitting was $4050 - 5550$ Å. The observed and best-fit model spectra are shown in Fig. 3.

To estimate the uncertainties for both of the velocity dispersion and the Lick indices (see below), we performed Monte Carlo simulations: The observed spectrum was altered with random modifications drawn from a normal distribution with a width according to the error spectrum. The modified spectrum was then fitted in the same way, and the steps were repeated 1000 (for the velocity dispersion) or 500 (for the Lick indices) times. The adopted values and their uncertainties are then given by the mean and standard deviation of Gaussian fits to the distribution of the individual fitted values.

2.3.1 Internal kinematics

The recession velocity and velocity dispersion were determined with the best-fitting template by pPXF. We discarded the calcium (Ca-)triplet lines due to a lack of a sufficiently high resolution stellar library for this spectral range. For the final velocity dispersion and its uncertainty we adopted from the Monte Carlo simulation of the fitting process, i.e. $\sigma_{ap} = 27 \pm 2$ km s^{-1}. Therefore, we obtained a realistic estimate for the uncertainty in the velocity dispersion as demonstrated in Fig. 4. Also, systematic errors from template mismatch were minimised by using a large library of template stars. Using velocity standard stars (a small number from our observing run, and those from Haşegan et al. 2005) observed with the same setup, for a similar wavelength range as well as for the Ca-triplet, led to consistent velocity dispersions but larger uncertainties (for comparisons with the Haşegan et al. data see Section 3.3). We also note that the measured velocity dispersion is well above the instrumental resolution and Geha et al. (2002) found that it is feasible to reliably measure (with an accuracy of 10%) velocity dispersions ($\sigma \sim 18.5$ km s^{-1}) below the instrumental

Table 3. Literature values and our measurements for S999

Quantity	Literature	This study
Magnitude		
$M_{g,AB}$	-10.791 (H05)	-10.79 ± 0.06
$M_{i,AB}$	-11.44 (S11)	—
$M_{z,AB}$	-11.711 (H05)	-11.69 ± 0.06
M_V	-11.16 (M13)	—
$M_{F606W(V)}$	—	-11.40 ± 0.06
$M_{F814W(I)}$	—	-12.13 ± 0.06
M_{K_s}	—	-13.4 ± 0.03
Size [pc]		
$R_{e,g}$	19.9 ± 0.2 (H05)	20.2 ± 1.0
$R_{e,i}$	34.1 (S11)	—
$R_{e,z}$	21.9 ± 0.5 (H05)	22.0 ± 1.1
$R_{e,F606W(V)}$	—	20.8 ± 1.0
$R_{e,F814W(I)}$	—	21.3 ± 1.1
Velocity dispersion [km s^{-1}]		
σ_{ap}	23.3 ± 1.3 (H05)	27 ± 2
σ_{tot}	—	26 ± 2
σ_0	25.6 ± 1.4 (H05)	—
σ_0	23.2 ± 1.3 (M13)	—
σ_0	26.2 ± 1.3 (MB14)	—
Metallicity		
$[\mathrm{Fe/H}]_{gz}$	-1.93 (H05)	—
$[\mathrm{Fe/H}]_{CT_1}$	-1.38 (H05)	—
[Fe/H]	-1.40 (M13)	—
$[\mathrm{Fe/H}]_{spec}$	—	-1.27 ± 0.12
Age [Gyr]	—	$7.6^{+2.0}_{-1.6}$
Mass [10^6 $M_\odot$]		
M_{dyn}	24.3 ± 2.7 (M13)	
M_{dyn}	22.4 ± 3.0 (H05)[6]	32 ± 5
M_{dyn}	21.2 (F14)	
M_*	2.6 (F14)	$3.9^{+0.9}_{-0.6}$
M_*	5.6 (M13)	
Ratios		
M_*/L_z	—	$1.3^{+0.3}_{-0.2}$
M_{dyn}/M_*	8.5 (F14)	5.6...**8.2**...11.2
M_{dyn}/M_*	4.45 ± 0.87 (M13)	

The references in the Table are: H05 – Haşegan et al. 2005; S11 – Strader et al. 2011; M13 – Mieske et al. 2013, using H05 data; MB14 – Mieske & Baumgardt 2014, priv. comm.; F14 – Forbes et al. 2014; the values were converted to our assumed distance of 16.7 Mpc when necessary. The velocity dispersion σ_{tot} is from the mass modelling, integrating over the whole object. For the mass ratio we list our preferred value (bold), as well as the range from lower/upper estimates for dynamical and stellar mass.

resolution with a similar setup and lower signal-to-noise ratio.

2.3.2 Stellar populations

In order to derive stellar population parameters, we measured Lick indices according to the definition of Trager et al. (1998). The measured indices are corrected to the Lick resolution by multiplying the index measured on the observed spectrum I_{Obs} with the ratio of the index measured on the best-fit model convolved to the observed velocity dispersion ($I^{\mathrm{Obs}}_{\mathrm{best}}$) and the Lick resolution ($I^{\mathrm{Lick}}_{\mathrm{best}}$):

$$I_{\mathrm{Corr}} = I_{\mathrm{Obs}} \frac{I^{\mathrm{Lick}}_{\mathrm{best}}}{I^{\mathrm{Obs}}_{\mathrm{best}}}. \quad (1)$$

The Lick resolution for each index is taken from Schiavon et al. (2005), and for the convolution the template resolution with a FWHM of 0.55 Å was subtracted in quadrature.

We interpolated the Thomas et al. (2011) single stellar population (SSP) models to a fine grid (steps of 0.02 dex in each direction; Onodera et al. 2014) of age, metallicity ([Z/H]), and α-abundance ([α/Fe]) in order to find the SSP-equivalent stellar population parameters of S999 via χ^2 minimisation,

$$\chi^2 = \frac{(I_{\mathrm{Thomas}} - I_{\mathrm{Measured}})^2}{\sigma^2_{\mathrm{Index}}} \quad (2)$$

where σ_{Index} is the 1σ uncertainty of the index derived from Monte Carlo simulations.

The indices included in the analyses were Hδ_{A}, Ca4227, G4300, Hγ_{A}, Hγ_{F}, Fe4383, C$_2$4668, Mg$_1$, Mg$_2$, Mgb, Fe5270, Fe5335, and Fe5406. The other indices in the wavelength range (H$_{\delta_F}$, CN1, CN2, Ca4455, Fe4531, H$_\beta$, Fe5015, Fe5709, Fe5782, NaD, TiO$_1$, TiO$_2$) were excluded since they are either not well calibrated in the model or significant outliers in the model comparisons. In the comparison of observed and bestfit spectrum (Fig. 3) there are some notable broader deviations (e.g. around 4150 Å, 4600 Å, and 4800 Å). These are caused by combining the various Echelle orders with imperfect corrections for the blaze function, resulting in a slight mismatch of the spectra's slopes in the overlap region of a pair of subsequent orders. It is possible that only the C$_2$4668 and H$_\delta$ indices are affected. Omitting those or using a slightly different blaze correction obtained from a different star do not change any of our conclusions.

We obtain: Age $= 7.6^{+2.0}_{-1.6}$ Gyr; $[Z/\mathrm{H}] = -0.95^{+0.12}_{-0.10}$; $[\alpha/\mathrm{Fe}] = 0.34^{+0.10}_{-0.12}$; [Fe/H] $= -1.27 \pm 0.12$ (assuming [Fe/H] $= [Z/\mathrm{H}] - 0.94[\alpha/\mathrm{Fe}]$, Thomas et al. 2003). The predicted model colours $F606W(V) - F814W(I) = 0.72$ and $(g-z)_{AB} = 1.04$ for an age of 8 Gyr and metallicity $[Z/\mathrm{H}] = -0.95$ are in good agreement with the observed integrated colours of $F606W(V) - F814W(I) = 0.73 \pm 0.08$ and $(g-z)_{AB} = 0.90 \pm 0.08$ (Fig. 2).

The colour gradient is a hint that the stellar population of S999 may not be well represented by the assumption of a simple stellar population. In order to estimate the effect on the stellar mass-to-light ratio of a more complex star formation history we used a model grid with the combination of two simple stellar populations: we combined the SSPs of Thomas et al. (2011) with the model of a population of an age of 15 Gyr, $[Z/\mathrm{H}] = -2.25$, and $[\alpha/\mathrm{H}] = 0.3$, with a mass fraction of 10% to 90% in steps of 10%. The indices in the combined model were calculated as luminosity weighted averages using the mass-to-light ratios of Maraston (2005). The smallest χ^2 was achieved with half of the mass in each of the populations. The young population was then fitted with an age of $4.5^{+3.5}_{-1.7}$ Gyr, $[Z/\mathrm{H}] = -0.10^{+0.30}_{-0.25}$, and $[\alpha/\mathrm{Fe}] = 0.10^{+0.10}_{-0.15}$. The total stellar mass for this model is slightly

[6] Obtained via a fit of a King model.

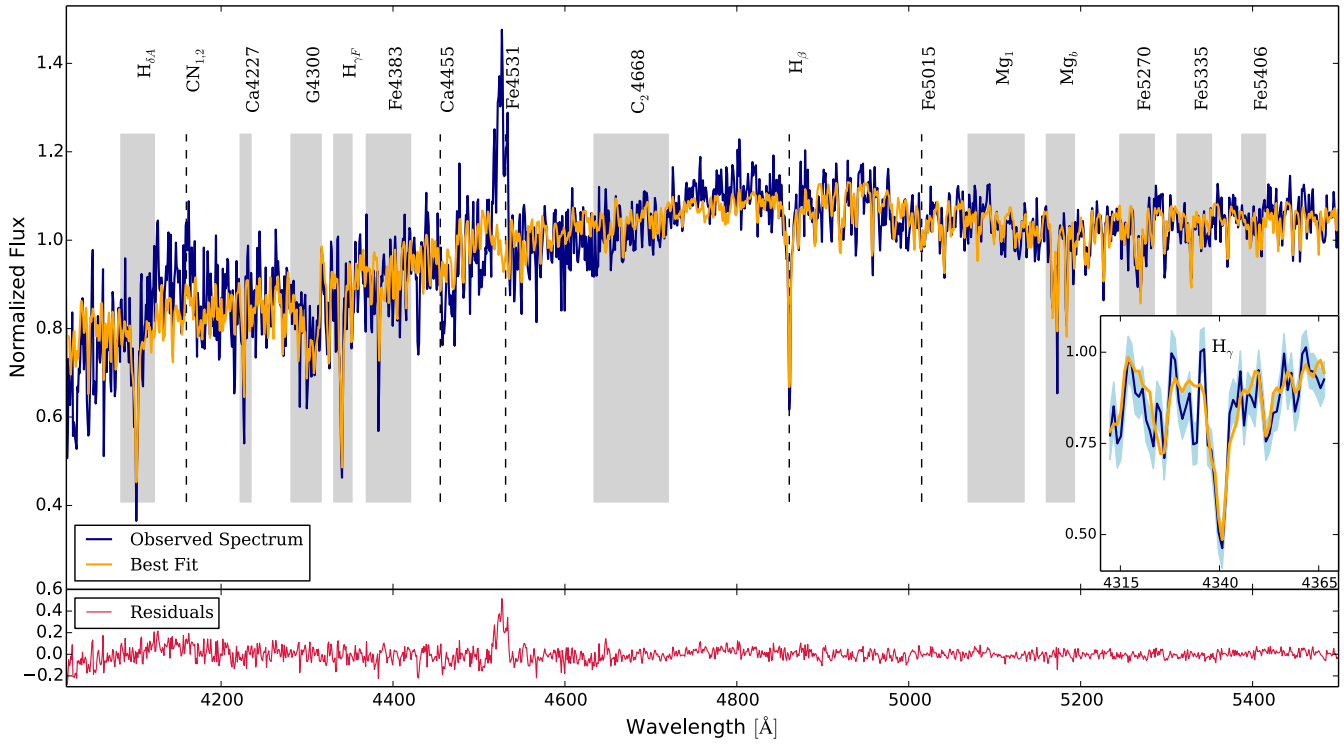

Figure 3. Spectrum of S999 in the rest frame. The *top* panel shows the observed spectrum (blue line, shifted to the rest frame) and the bestfit template obtained with pPXF (orange line). The grey shaded regions indicate the pass bands of indices used in the determination of age and metallicity (omitting $H_{\gamma A}$ and Mg_2, which overlap with $H_{\gamma F}$ and $Mg\,b$, respectively), while the remaining indices are indicated with the dashed horizontal lines. A zoom in on the H$_\gamma$ line in the inset shows the quality of the fit, with the light blue shaded area indicating the uncertainty of the observed spectrum. The residuals are shown in the *bottom* panel (red line). The residual around 4530 Å is caused by a bad column in the detector. We exclude the Fe4531 index, when fitting for the stellar population parameters, since it coincides with some faulty pixels of the detector.

larger than the SSP-equivalent, but not by a lot: $M_* = 4.1 \times 10^6 M_\odot$ and actually within the SSP stellar mass uncertainty.

3 RESULTS AND DISCUSSION

3.1 Light profile

All eight analysed UCDs follow single Sérsic profiles quite well, although two of them show deviations at a surface brightness around 20 to 21 mag arcsec^{-2} in the I band (see also Appendix A). S999 is the only object with a small excess of light in the outer parts, which is significant in both bands after taking measurement and background subtraction uncertainties into account (Fig. 2). However, the excess is at a low surface brightness level of $\sim$ 24-25 mag arcsec^{-2} in I and V, respectively (the excess contributes only a small fraction of the total light, i.e. $\sim$ 2%). For comparison, the two Sérsic components of VUCD7 (Evstigneeva et al. 2008) contribute equally to the surface brightness of $\mu_V \approx 20.6$ mag arcsec^{-2} at $r \approx 0\farcs4$.

The size of S999 based on the Sérsic fit to the surface brightness profile might be underestimated, since the image was not deconvolved, even though the innermost region was excluded from the fit. However, the obtained size is consistent with literature values (see Table 3), with the exception of Strader et al. (2011), who fitted a King model with fixed concentration.

At least three UCDs – S999, S887, and S5065 – have colour profiles that become steadily bluer towards larger radii over a range with a reliable colour measurement, by about ~ 0.15 mag. Again, the uncertainty of the background subtraction is the major limitation. However, the colour profiles are consistent with the $g-z$ profiles measured from the ACS VCS images. Evstigneeva et al. (2008) found similar positive colour gradients for the brightest UCDs in their sample.

We note that the fourth cosine term profile, i.e. disky or boxy isophotes, does not reveal any significant features correlated with the surface brightness profile of S999 (not shown).

3.2 Extreme mass ratio

We determined the dynamical mass of S999 by assuming it is perfectly described as a Sérsic function. Since the size has a slight wavelength dependence, we used an average value of those radii from the Sérsic fits to surface brightness profiles in $F606W$ and $F814W$ ($R_e = 20.9$ pc). Using the equations in Ciotti (1991), we deprojected the observed Sérsic function to create a smooth three-dimensional density distribution. We assumed an initial mass normalisation and calculated the resulting projected velocity dispersion as a function of projected radius. From the density distribution we sampled 10^6 stars, calculated their projected radii, and assigned each

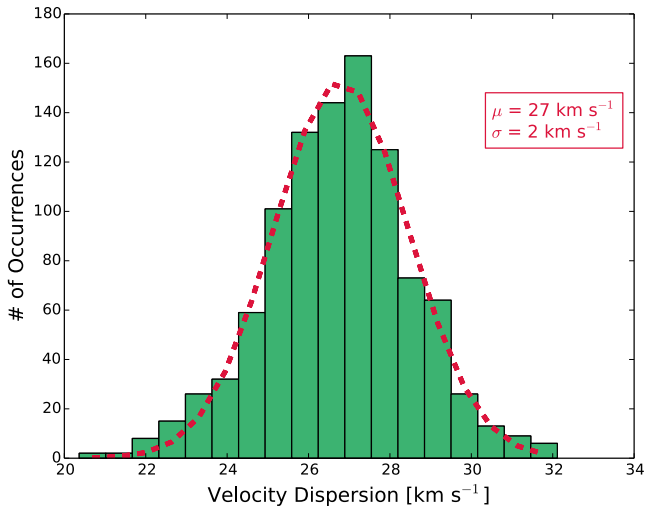

Figure 4. Distribution of velocity dispersion values of S999 from 1000 Monte Carlo simulations, simulating random artificial noise according to the error spectrum. We adopt the values for the velocity dispersion and its uncertainty as the centre and sigma (see box) from a Gaussian fit to the distribution (red dashed line).

star a velocity along the line of sight consistent with the projected dispersion at that projected radius. We convolved each star with a Gaussian assuming a FWHM of the seeing ($0\farcs6 \sim 48.6$ pc). We then projected the angular dimensions of the slit ($0\farcs75 \times 2\farcs5$) to the distance of S999 and integrated each stellar seeing disk over the slit. We next calculated the observed integrated velocity dispersion within the slit, using the slit integration factors as weights in the integrated dispersion. Finally, we scaled the mass normalisation appropriately until the modelled integrated velocity dispersion σ within the slit matched the observed value.[7] The resulting total dynamical mass is $M_{dyn} = 32 \pm 5 \times 10^6 M_\odot$. Given the large number of stars used in the simulation, we found that the random uncertainty in the total dynamical mass is dominated by the uncertainty in the measured velocity dispersion and that sampling uncertainties are not important.

For the conversion from luminosity to stellar mass we took the stellar mass-to-light ratios assuming a Kroupa IMF from Maraston (2005), which are valid for the Thomas et al. (2011) stellar population models, which we used.[8] We chose to use the z-band, since the mass-to-light ratio depends less critically on the age, [Z/H], and [α/Fe] of the stellar populations at longer wavelengths. The uncertainty of the total luminosity in the z-band with lower S/N as compared to e.g. $F814W$ is still small, and the model M/L is readily available. Interpolating the model stellar mass-to-light ratios resulted in approximately $M/L_z = 1.1$ to 1.6 for our observed age and metallicity including the ranges of uncertainty. The best guess is $M/L_z = 1.3$, which results in a stellar mass of $M_* = 3.9 \times 10^6 M_\odot$ ($M_* = 3.3$ to $4.8 \times 10^6 M_\odot$ for the range of mass-to-light ratios).

Furthermore, we converted the ground-based K_s magnitude into stellar mass, benefitting from the even longer wavelength. With the measured age and metallicity, Maraston (2005) yielded $M/L_{K_s} = 0.8 \pm 0.1$ (the range comes again from the uncertainties in age, [Z/H], and [α/Fe]) and a stellar mass of $M_* = 3.8^{+0.6}_{-0.5} \times 10^6 M_\odot$. Using the Bressan et al. (2012, 2013) models and the procedure described in Norris et al. (2014b) gave a slightly larger, but consistent mass of $M_* = 4.7^{+0.9}_{-0.6} \times 10^6 M_\odot$. In both cases the uncertainties are dominated by those of the measured stellar population age. Both measurements are in good agreement with the stellar mass derived from *HST* imaging ($3.9 \times 10^6 M_\odot$).

The resulting dynamical-to-stellar mass ratio is $\sim$8. The range of possible mass ratios is rather large, due to the uncertainties in both the stellar mass-to-light ratio and the dynamical mass estimate (i.e. 5.6 to 11.2 with the lowest dynamical and highest stellar mass and vice versa). However, the mass ratio remains elevated even when adopting a stellar mass at the high end ($M_* = 4.8 \times 10^6 M_\odot$) of the possible range and scaling the dynamical mass down to the lowest published velocity dispersion ($\sigma = 20$ km s^{-1}; Haşegan et al. 2005 using `fxcor`), i.e. $M_{dyn}/M_* \geqslant 3.7$.

3.3 Comparison to literature

An extreme mass ratio has previously been calculated for S999 (Haşegan et al. 2005; Mieske et al. 2008b; Forbes et al. 2014), all based on the ESI spectrum of Haşegan et al.. With improved photometry from deeper images (factor $\sim$60 in total integration time), and new spectroscopy (factor $\sim$5 in total integration time) allowing for additional constraints on the stellar population we confirm that the mass ratio is indeed elevated.

Haşegan et al. (2005) measured the velocity dispersion of S999 in two different ways: with cross-correlation and with pPXF. Their two measurements are not compatible with each other ($\sigma_{ap} = 19.6 \pm 1.0$ km s^{-1} and $\sigma_{ap} = 25.6 \pm 1.4$ km s^{-1}, respectively), but this might be explained by an underestimation of the uncertainty. We note that for both their methods Haşegan et al. used five stars, which were observed with the same setup. Here we made use of the much larger library of high resolution ELODIE stellar templates, which were observed with a different instrument. Repeating their measurement with pPXF around the magnesium triplet region, we reproduce their velocity dispersion, but obtain a 2-5 times larger uncertainty $\sigma_{ap} = 24.5 \pm 3.5$ km s^{-1}, which is not accounting for systematic uncertainties. The velocity dispersion measurement using our own spectrum agrees well with that of Haşegan et al. when using pPXF (as we do). Given our uncertainty estimate, which is larger than that of Haşegan et al. for their spectrum with 5 times shorter total integration time, our updated larger estimate for the uncertainty of the data with a smaller signal-to-noise ratio seems consistent, showing the usefulness of the Monte Carlo simulation for a realistic estimate.

Our size measurements for the ACS VCS pointings are in good agreement with those of Haşegan et al. (2005), even though our approach was simpler in the sense that

[7] Our mass modelling is basically following Hilker et al. (2007). However, they truncated the profiles at 500 pc (H. Baumgardt, priv. comm.). The resulting dynamical masses are slightly smaller than they would be without the truncation, with the difference depending on the profile. For example for the Fornax UCD4 ($R_e = 24.1$ pc, $n = 5.5$, Evstigneeva et al. 2007) it is a 3% effect.

[8] Which horizontal branch morphology (blue or red) is assumed for the lowest metallicity models has no influence on our mass-to-light ratios in the z- and K_s-bands.

we excluded the innermost region from the fit of the surface brightness profile instead of taking into account the convolution by the PSF as Haşegan et al. did. Also, the radii measured on the deeper images are very consistent. All of the measurements follow the mild trend to larger radii at longer wavelengths, consistent with the colour gradient of S999. Strader et al. (2011) obtained a larger size using a King profile with fixed concentration. The Mieske et al. (2013) effective radius is the average of the Haşegan et al. (2005) radii in the two filter bands, just as we use the average of the radii from the two deep images.

Haşegan et al. (2005) calculated the dynamical mass from their King model fit to the ACS VCS surface brightness profile, using the central velocity dispersion, which they obtained from the expected velocity dispersion profile by taking into account the seeing. Mieske et al. (2013) corrected the calculation of Haşegan et al. to the proper King core radius and obtained a slightly larger dynamical mass estimate. Our dynamical mass for S999 is larger than both these values, but in agreement within the uncertainties with the corrected mass estimate by Mieske et al. (2013) (see Table 3).

The magnitudes show an excellent agreement with Haşegan et al. (2005), better than our estimate of their uncertainty. Their contribution to the uncertainty of the mass ratio is smaller than that of any of the other parameters.

Haşegan et al. (2005) did not calculate the mass ratio and quoted the dynamical mass-to-light ratio instead. They listed two metallicity estimates for S999, based on the ACS VCS $g-z$ colour and a $C-T_1$ colour, respectively. While the former is lower than our measurement, the latter is reasonably close. For calculating the stellar mass, Mieske et al. (2013) assumed an age of 13 Gyr and extrapolated the Maraston (2005) stellar mass-to-light ratios for S999's metallicity (they used $[Fe/H]=-1.4$) to get $M/L_V=2.2$. Forbes et al. (2014) used the stellar mass of Norris et al. (2014a), which used $M/L_V=1.1$ (or effectively, with S999's metallicity, an age of about 3.5 Gyr). While we chose to use the z-band instead of the V-band, the mass-to-light ratio in the V-band for the stellar populations we find is $M/L_V\sim1.7$.

As we have seen, the dynamical mass estimates for S999 span a range of values, but agree within the uncertainties. The other main driver for the large range of values for the dynamical-to-stellar mass ratio (a factor of ∼2 between the lowest and highest estimate) is the characterisation of the stellar populations. Our stellar mass-to-light ratio lies in-between the estimates of Mieske et al. (2013) and Forbes et al. (2014). Also our preferred mass ratio is in-between the extremes of these two studies. However, in comparison to those, we clearly improved the characterisation of the stellar populations with the ESI spectrum. Also with the better constrained stellar mass the dynamical-to-stellar mass ratio of S999 remains elevated, i.e. with the preferred value of $M_{dyn}/M_*=8.2$ and a range from 5.6 to 11.2.

3.4 Elevated mass ratios in UCDs

Our mass ratio of ∼8 implies either an underestimated stellar mass or extra mass that contributes to the dynamical mass without adding light. In the following we discuss possible explanations for an elevated mass ratio in S999 and in UCDs in general.

3.4.1 Non-canonical initial mass function

If the initial mass function (IMF) differs from the assumed one, then the inferred stellar mass changes, mostly increases. This is true for both top and bottom-heavy IMFs, since stellar remnants of massive stars add mass but no light, and low-mass stars contribute mass, while adding very little light. Both cases have been suggested to explain the elevated mass ratios in UCDs (e.g. Dabringhausen et al. 2008; Mieske et al. 2008a).

However, by changing the assumed IMF, the fitted SSP age and metallicity will also be altered. In order to estimate the combined effect on the mass-to-light ratio we fitted MILES SSP models with varying IMF slope (Vazdekis et al. 2010, with slopes from 0.3 to 3.3, solar α-abundances). With increasing slope, the fitted age generally also increases (as well as χ^2), while the metallicity decreases. The Vazdekis et al. models are provided for IMFs with a power-law and a broken power-law (with the slope varying for stars with $M>0.6M_\odot$, see Appendix A of Vazdekis et al. 2003 for details). Relative to the assumption of a Kroupa IMF the mass-to-light ratio increases by about a factor of three for the broken power-law IMF with the steepest slope for high-mass stars (and by about a factor of four for the shallowest). Using a single power-law IMF, the mass-to-light increases by a factor of about 3 for a slope of 2.3 as compared to a Salpeter IMF (slope 1.3 in Vazdekis et al.'s parametrisation, with an increased mass-to-light ratio by about a third as compared to the Kroupa IMF; the shallowest single power-law IMF with a slope of 0.3 results in an increase by a factor 2 to 3). Formally, a single power-law IMF with a slope of around 3.3 would result in a mass-to-light ratio sufficient to account for the dynamical mass. However, again formally, the models with shallower slopes should be preferred, since the models with slopes steeper than 2.3 let the χ^2 increase dramatically (by a factor of more than >24 for a slope of 3.3).[9] We note that such a slope is also beyond any observed IMF slope for the most massive galaxies (e.g. Cappellari et. al. 2012; Spiniello et al. 2012; Conroy & van Dokkum 2012). Assuming that similar factors for the mass-to-light ratios would result from varying the IMF in the Thomas et al. (2011) models, which we used for our mass-to-light estimation in order to account for the α-enhancement, we conclude that none of the reasonable fits yields a mass-to-light ratio sufficient to result in a dynamical-to-stellar mass ratio of unity.

We note that Frank (2014) did not find any evidence for a bottom-heavy IMF in S999 (nor S928), using the CO index. However, their uncertainties were too large to completely rule out a bottom-heavy IMF. Recently, Dabringhausen et al. (2012) claimed that UCDs have high rates of X-ray binaries, indicative of of an overpopulation of remnants of massive stars (however, Phillipps et al. 2013 find the opposite for Fornax UCDs). We do not find any of the X-ray sources of Jordán et al. (2004, with an X-ray completeness limit of $L_X\sim5\times10^{39}$ erg s^{-1}) to coincide with the position of any of our 8 UCDs. However, this does not put firm constraints on the number of low-mass X-ray binaries and the remnants of massive stars. Thus, we conclude that

[9] This most extreme model reverts the trend of fitted age increasing with the IMF slope, and results in the youngest fitted age, possibly as well indicating that the fit is not reliable.

the elevated mass ratio of S999 is unlikely explained with a bottom-heavy IMF, but may have a contribution from an excessive number of stellar remnants from a top-heavy IMF.

3.4.2 Central massive black hole

Mieske et al. (2013) showed that on average a massive black hole with a mass of about 15% of the UCD stellar mass could explain the generally elevated mass ratios seen in UCDs, and is consistent with progenitor galaxies having a total mass of about $10^9 M_\odot$. For S999 they calculated the mass of the central black hole to be $M_{BH} = 25 \times 10^6 M_\odot$, several times the stellar mass, in order to explain their mass ratio for S999. This would make S999 the most black hole dominated UCD or galaxy known by far.

Seth et al. (2014) have confirmed a massive black hole in M60-UCD1 (note that M60-UCD1's mass ratio was not previously found to be elevated based on its unresolved velocity dispersion). This kind of data, however, is currently rare. Frank et al. (2011) did not find evidence for a massive black hole in UCD3 (a UCD in the Fornax cluster which does not have an elevated mass ratio). The non-detection of S999 in the X-rays cannot rule out a massive black hole, but requires that it is non-accreting. Integral field spectroscopy with high spatial resolution will allow one to detect the central black hole dynamically, or to put limits on its mass.

3.4.3 Tidal Stripping

Forbes et al. (2014) argued with the stripping simulations of Pfeffer & Baumgardt (2013) that the early stages of the tidal stripping process may be an explanation for the observed extreme mass ratios seen in half a dozen UCDs, including S999. The mass ratios in the stripping simulations are reduced when taking into account the variation of velocity dispersion and virial coefficient (Pfeffer, priv. comm.), instead of assuming them to be constant like Forbes et al. (2014) did. While they remain elevated, this puts even stronger constraints on the specific orbits that can cause stripping to be strong enough to explain the extreme mass ratios. If stripping is the cause of the elevated mass ratio we would expect the UCDs to reveal extra halo light in their surface brightness profiles. Our results presented here indicate that S999 has little if any extra halo light beyond a single Sérsic profile. Thus we conclude it is unlikely that the extreme mass ratio of S999 is completely due to it currently undergoing tidal stripping. Several other UCDs with two-component structures (VUCD7, UCD3, UCD5, FCC303, M60-UCD1, M59cO; Haşegan et al. 2005; Drinkwater et al. 2003; Chilingarian & Mamon 2008; Evstigneeva et al. 2008; Chiboucas et al. 2011), possibly including two of the UCDs in our sample (S928 and S8005, see Appendix A), are more likely candidates, and may suggest a continuity from nucleated galaxies via UCDs with envelopes to single component UCDs.

However, stripping is still part of the explanation, if a central massive blackhole inherited from the more massive progenitor galaxy which had been stripped, is responsible for the elevated mass ratio. Also, the positive colour gradients found for S999 and some of the other analysed UCDs might be expected from the stripping scenario: the assumed progenitors, which were nuclei of early-type dwarf galaxies, typically have bluer colours than the host galaxy (Lotz et al. 2004; Côté et al. 2006; Turner et al. 2012; den Brok et al. 2011). Generally, early-type galaxies with masses of the potential progenitors do not show negative colour gradients (as seen in more massive galaxies) but often have positive gradients (Tortora et al. 2010), generally interpreted as age gradients. The remnants in the stripping simulations of Pfeffer & Baumgardt (2013) are larger in size than the nuclei of the progenitor galaxies. The authors did not attribute this increase in size to dynamical heating of the nucleus, but rather to stars from the progenitor remaining in the remnant. As these stars are expected to be typically found at larger radii than the stars of the nucleus, the observed positive colour gradient might be expected. The typical difference in colour between the nucleus and the main body of the galaxy (e.g. Côté et al. 2006; den Brok et al. 2011) is similar to the typical observed colour gradient in UCDs.

While Evstigneeva et al. (2008) argued that the levels of α-enhancements in UCDs and nuclei are not consistent with the stripping scenario, Paudel et al. (2010) found them to be similar when comparing nuclei and UCDs at similar local projected galaxy density. The level of α-enhancement in S999 is similar to that of Paudel et al.'s high local density UCDs.

3.4.4 Dark Matter

Haşegan et al. (2005) suggested (non-baryonic) dark matter as a possible explanation for the elevated mass ratio of S999. However, Murray (2009) argued that, by comparison to the central dark matter densities of theoretical dark matter profiles and observed Local Group dwarf spheroidals, dark matter cannot contribute large amounts of mass in UCDs. Typically, the dark matter fraction within the half-light radius is expected to be less than 30% (see also Tollerud et al. 2011; Seth et al. 2014).

In their stripping simulations, Pfeffer & Baumgardt (2013) assumed that the progenitor galaxy is largely stripped of dark matter before the stars can be affected, and did not include any dark matter. Baumgardt & Mieske (2008) showed that mass segregation in compact stellar systems will expel dark matter particles from the dense central regions of these objects. However, the authors calculated that the time scale for this process is larger than a Hubble time for UCDs.

We conclude that, while S999 is a good candidate to search for dark matter in UCDs thanks to its low stellar density compared to other UCDs, dark matter should not play a major role in explaining the elevated mass ratio.

4 SUMMARY

We used our measurements of size ($R_e = 20.9 \pm 1.0$ pc) and velocity dispersion ($\sigma_{ap} = 27 \pm 2$ km s^{-1}) based on high-quality data to determine the dynamical mass ($M_{dyn} = 32 \pm 5 \times 10^6 M_\odot$) of the ultra-compact dwarf (UCD) S999 via mass modelling. Furthermore, we newly obtained stellar population characteristics (Age $= 7.6^{+2.0}_{-1.6}$ Gyr; $[Z/\mathrm{H}] = -0.95^{+0.12}_{-0.10}$; $[\alpha/\mathrm{Fe}] = 0.34^{+0.10}_{-0.12}$), and calculated the stellar mass $M_* = 3.9^{+0.9}_{-0.6} \times 10^6 M_\odot$ assuming a Kroupa stellar initial mass function (IMF). With these new independent mea-

surements we derived the dynamical-to-stellar mass ratio of S999 $M_{dyn}/M_* = 8.2$. Furthermore, we estimated realistic uncertainties of the measurements, and considered the possible ranges of the values. We confirmed the mass ratio to be elevated beyond what is expected from stellar populations with a canonical IMF for the whole range of possible values $5.6 \leqslant M_{dyn}/M_* \leqslant 11.2$.

This elevated mass ratio can potentially offer insights to the formation of S999 and other UCDs, and we discussed possible, non-exclusive explanations. New measurements, e.g. of IMF-sensitive features of the spectrum and high-resolution integral field spectroscopy, are needed to explore the contributions of the listed possibilities.

We conclude that the most likely options include a central massive black hole (as recently found in M60-UCD1), and that the object is not in equilibrium so that the mass estimate based on the velocity dispersion is not adequate. Both might be related to S999 being the remnant nucleus of a tidally stripped progenitor galaxy, which could also explain its positive colour gradient. Most likely a combination of several of the explanations is required to explain the extreme value of the mass ratio of S999, since none of the possibilities alone is likely to account for all of the excess dynamical mass compared to the mass in stars.

ACKNOWLEDGMENTS

The authors thank the referee for helpful comments. They also thank M. Onodera for providing the code for interpolating the stellar population models, and T. Lisker for the non-parametric photometry code. JJ also thanks M.T. Murphy and J. Pfeffer for useful discussions about reduction of spectra and stripping simulation, respectively. JJ and DAF thank the ARC for financial support via DP130100388. Based on observations obtained with WIRCam, a joint project of CFHT, Taiwan, Korea, Canada, France, at the Canada-France-Hawaii Telescope (CFHT) which is operated by the National Research Council (NRC) of Canada, the Institut National des Sciences de l'Univers of the Centre National de la Recherche Scientifique of France, and the University of Hawaii.

REFERENCES

Bassino L. P., Muzzio J. C., Rabolli M., 1994, ApJ, 431, 634
Baumgardt H., Mieske S., 2008, MNRAS, 391, 942
Bekki K., Couch W. J., Drinkwater M. J., 2001, ApJ, 552, L105
Bertin E., Arnouts S., 1996, A&AS, 117, 393
Bird S., Harris W. E., Blakeslee J. P., Flynn C., 2010, A&A, 524, 71
Blakeslee J. P., et al., 2009, ApJ, 694, 556
Bressan A., Marigo P., Girardi L., Salasnich B., Dal Cero C., Rubele S., Nanni A., 2012, MNRAS, 427, 127
Bressan A., Marigo P., Girardi L., Nanni A., Rubele S., 2013, 40th Liège International Astrophysical Colloquium. Ageing Low Mass Stars: From Red Giants to White Dwarfs, 43, 03001
Brodie J. P., Romanowsky A. J., Strader J., Forbes D. A., 2011, AJ, 142, 199
Brodie J. P., et al., 2014, ApJ, 796, 52
Cappellari M., Emsellem E., 2004, PASP, 116, 138
Cappellari M., et al. 2012, Nature, 484, 485
Chiboucas K., et al., 2011, ApJ, 737, 86
Chilingarian I. V., Mamon G. A., 2008, MNRAS, 385, L83
Chilingarian I. V., Mieske S., Hilker M., Infante L., 2011, MNRAS, 412, 1627
Ciotti L., 1991, A&A, 249, 99
Conroy C.& van Dokkum P. G., 2012, ApJ, 760, 71
Côté P., et al., 2004, ApJS, 153, 223
Côté P., et al., 2006, ApJS, 165, 57
Dabringhausen J., Hilker M., Kroupa P., 2008, MNRAS, 386, 864
Dabringhausen J., Kroupa P., Baumgardt H., 2009, MNRAS, 394, 1529
Dabringhausen J., Fellhauer M., Kroupa P., 2010, MNRAS, 403, 1054
Dabringhausen J., Kroupa P., Pflamm-Altenburg J., Mieske S., 2012, ApJ, 747, 72
den Brok M., et al., 2011, MNRAS, 414, 3052
Drinkwater M. J., Jones J. B., Gregg M. D., Phillipps S., 2000, PASA, 17, 227
Drinkwater M. J., Gregg M. D., Hilker M., Bekki K., Couch W. J., Ferguson H. C., Jones J. B., Phillipps S., 2003, Nature, 423, 519
Evstigneeva E. A., et al., 2008, AJ, 136, 461
Evstigneeva E. A., Gregg M. D., Drinkwater M. J., Hilker M., 2007, AJ, 133, 1722
Forbes D. A., Lasky P., Graham A. W., Spitler L., 2008, MNRAS, 389, 1924
Forbes D. A., Norris M. A., Strader J., Romanowsky A. J., Pota V., Kannappan S. J., Brodie J. P., Huxor A., 2014, MNRAS, 444, 2993
Frank M. J., 2014, Astron. Nachr., 335, 486
Frank M. J., Hilker M., Mieske S., Baumgardt H., Grebel E. K., Infante L., 2011, MNRAS, 414, L70
Geha M., Guhathakurta P., & van der Marel R. P. 2002, AJ, 124, 3073
Graham A. W., Driver S. P., 2005, PASA, 22, 118
Graham A. W., Driver S. P., Petrosian V., Conselice C. J., Bershady M. A., Crawford S. M., Goto T., 2005, AJ, 130, 1535
Hanes D. A., Côté P., Bridges T. J., McLaughlin D. E., Geisler D., Harris G. L. H., Hesser J. E., Lee M. G., 2001, ApJ, 559, 812
Haşegan M., et al., 2005, ApJ, 627, 203
Hilker M., Baumgardt H., Infante L., Drinkwater M., Evstigneeva E., Gregg M., 2007, A&A, 463, 119
Hilker M., Infante L., Vieira G., Kissler-Patig M., Richtler T., 1999, A&AS, 134, 75
Janz J., Lisker T., 2008, ApJ, 689, L25
Jedrzejewski R. I., 1987, MNRAS, 226, 747
Jordán A., et al., 2004, ApJ, 613, 279
Le Borgne J. F., et al., 2003, A&A, 402, 433
Lotz J. M., Miller B. W., Ferguson H. C., 2004, ApJ, 613, 262
Madrid J. P., Harris W. E., Blakeslee J. P., Gómez M., 2009, ApJ, 705, 237
Maraston C., 2005, MNRAS, 362, 799
Marino A. F., et al., 2014, MNRAS, 442, 3044

Mieske S., Hilker M., Infante L., 2002, A&A, 383, 823
Mieske S., Hilker M., Infante L., Jordán A., 2006, AJ, 131, 2442
Mieske S., Dabringhausen J., Kroupa P., Hilker M., Baumgardt H., 2008a, Astron. Nachr., 329, 964
Mieske S., et al., 2008b, A&A, 487, 921
Mieske S., Frank M. J., Baumgardt H., Lützgendorf N., Neumayer N., Hilker M., 2013, A&A, 558, 14
Muñoz R. P., et al., 2014, ApJS, 210, 4
Murray N., 2009, ApJ, 691, 946
Norris M. A., Kannappan S. J., 2011, MNRAS, 414, 739
Norris M. A., Meidt S., van de Ven G., Schinnerer E., Groves B., Querejeta M., 2014b, ApJ, 797, 55
Norris M. A., et al., 2014a, MNRAS, 443, 1151
Onodera M., et al., 2014, eprint arXiv:1411.5023
Paudel S., Lisker T., Janz J., 2010, ApJ, 724, L64
Peng E. W., et al., 2009, ApJ, 703, 42
Penny S. J., Forbes D. A., Conselice C. J., 2012, MNRAS, 422, 885
Petrosian V., 1976, ApJ, 209, L1
Pfeffer J., Baumgardt H., 2013, MNRAS, 433, 1997
Phillipps S., Young A. J., Drinkwater M. J., Gregg M. D., Karick A., 2013, MNRAS, 433, 1444
Prugniel P., Soubiran C., 2001, A&A, 369, 1048
Puget P., et al., 2004, in Moorwood A. F. M., Iye M., eds, Ground-based Instrumentation for Astronomy. Edited by Alan F. M. Moorwood and Iye Masanori. Proceedings of the SPIE. SPIE, pp 978–987
Schiavon R. P., Rose J. A., Courteau S., MacArthur L. A., 2005, ApJS, 160, 163
Schlafly E. F., Finkbeiner D. P., 2011, ApJ, 737, 103
Schlegel D. J., Finkbeiner D. P., Davis M., 1998, ApJ, 500, 525
Seth A. C., et al., 2014, Nature, 513, 398
Sheinis A. I., Bolte M., Epps H. W., Kibrick R. I., Miller J. S., Radovan M. V., Bigelow B. C., Sutin B. M., 2002, PASP, 114, 851
Spiniello C., Trager, S. C., Koopmans, L. V. E., Chen, Y. P., 2012, ApJ, 753, L32
Strader J., et al., 2011, ApJS, 197, 33
Strader J., et al., 2013, ApJ, 775, L6
Strom S. E., Strom K. M., Wells D. C., Forte J. C., Smith M. G., Harris W. E., 1981, ApJ, 245, 416
Thomas D., Maraston C., Bender R., 2003, MNRAS, 339, 897
Thomas D., Maraston C., Johansson J., 2011, MNRAS, 412, 2183
Tollerud E. J., Bullock J. S., Graves G. J., Wolf J., 2011, ApJ, 726, 108
Tortora C., Napolitano N. R., Cardone V. F., Capaccioli M., Jetzer P., Molinaro R., 2010, MNRAS, 407, 144
Trager S. C., Worthey G., Faber S. M., Burstein D., Gonzalez J. J., 1998, ApJS, 116, 1
Turner M. L., Côté P., Ferrarese L., Jordán A., Blakeslee J. P., Mei S., Peng E. W., West M. J., 2012, ApJS, 203, 5
Vazdekis A., Cenarro A. J., Gorgas J., Cardiel N., & Peletier R. F., 2003, MNRAS, 340, 1317
Vazdekis A., Sánchez-Blázquez P., Falcón-Barroso J., Cenarro A. J., Beasley M. A., Cardiel N., Gorgas J., & Peletier R. F., 2010, MNRAS, 404, 1639
Waters C. Z., Zepf S. E., Lauer T. R., Baltz E. A., 2009, ApJ, 693, 463
Webb J. J., Harris W. E., Sills A., 2012, ApJ, 759, L39
Wolf J., Martinez G. D., Bullock J. S., Kaplinghat M., Geha M., Muñoz R. R., Simon J. D., Avedo F. F., 2010, MNRAS, 406, 1220

APPENDIX A: LIGHT PROFILES OF UCDS CLOSE TO M87

In addition to S999 there are seven more UCDs in the ACS field of view. Here we present the surface brightness and colour profiles of the remaining UCDs. Most of the analysed UCDs follow single Sérsic profiles well (Fig. A1). While the proper subtraction of M87's light is non-trivial, the consistency of the profiles and their fits in the two filter bands is reassuring. Two UCDs, S928 and S8005, show a clear dip of the observed profile in comparison to the fitted profile (seen as a positive residual) at a surface brightness around 20 to 21 mag arcsec^{-2} in the I band.

The colour gradients in the UCDs are mostly positive. Again, the uncertainty of the background subtraction is the major limitation. However, the colour profiles are consistent with the $g-z$ profiles measured on the ACS VCS images. For at least three UCDs – S999, S887, and S5065 – the colours become steadily consistently bluer by about $\sim$ 0.15 mag towards larger radii over a range where the colours are reliable. The fourth cosine term profile, i.e. disky or boxy isophotes, does not generally display significant features correlated with the surface brightness profile – with the possible exception of S8005, which becomes disky in the outer parts ($C_4 \sim 0.04$).

Our photometric measurements of the UCDs in the ACS VCS pointing are given in Table A1.

Table A1. Imaging of UCDs from the ACS VCS

UCD	Non-parametric				Sérsic fit							
	F475W (g)		F850LP (z)		F475W (g)				F850LP (z)			
	m	a_e [″]	m	a_e [″]	m	a_e [″]	μ_e	n	m	a_e [″]	μ_e	n
S999	20.38	0.28	19.49	0.29	20.31	0.26	20.04	1.1	19.42	0.28	19.33	1.0
H44905	22.07	0.26	21.09	0.27	22.00	0.26	21.62	0.7	21.12	0.29	20.82	0.5
S887	21.29	0.17	20.23	0.19	20.92	0.13	19.41	2.0	19.93	0.16	18.94	2.1
S928	19.97	0.30	19.13	0.30	19.82	0.29	19.84	1.3	18.95	0.31	19.11	1.2
S5056	20.31	0.20	19.35	0.22	20.14	0.18	19.14	1.0	19.10	0.19	18.22	1.2
S8005	20.71	0.32	19.84	0.33	20.59	0.33	20.75	1.1	19.62	0.35	19.98	1.3
S8006	20.67	0.25	19.78	0.26	20.56	0.24	20.13	1.1	19.57	0.25	19.27	1.2

Same as Table 2, but for the ACS VCS images in the g and z-bands. S672 is outside the field of view.

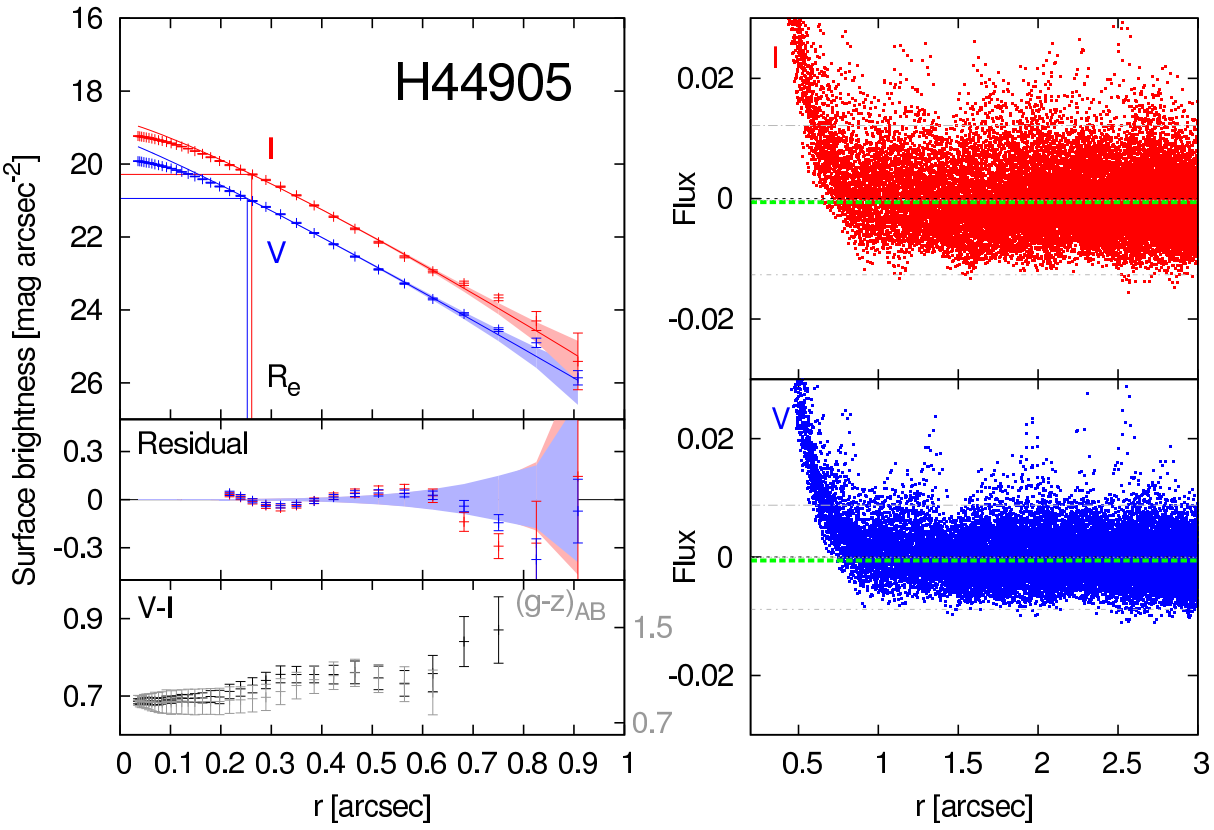

Figure A1. Surface brightness and colour profiles of UCDs around M87. Same as Fig. 2. The name of the UCD is given in the top left panel.

Figure A1 – *continued*

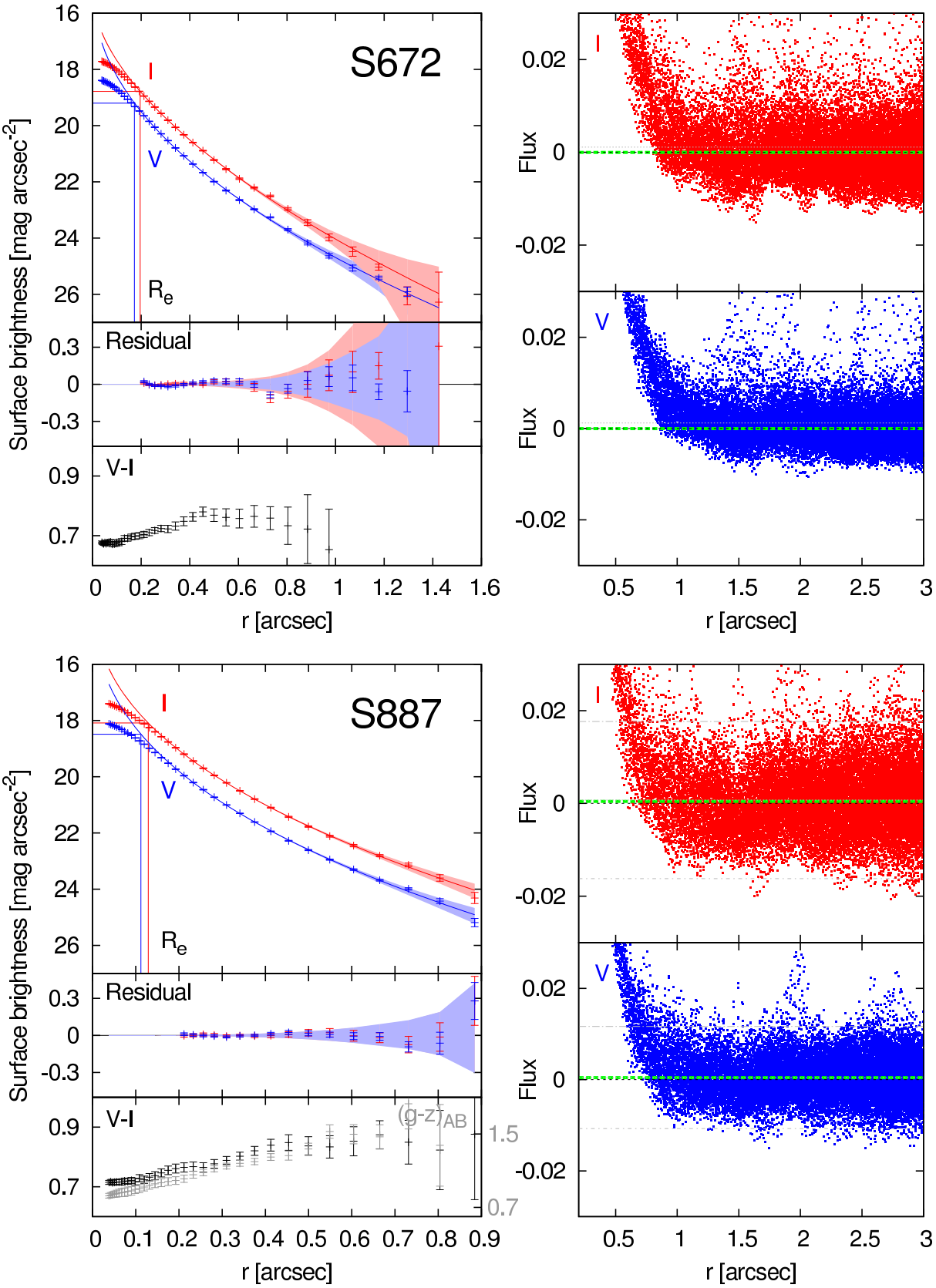

Figure A1 – *continued*

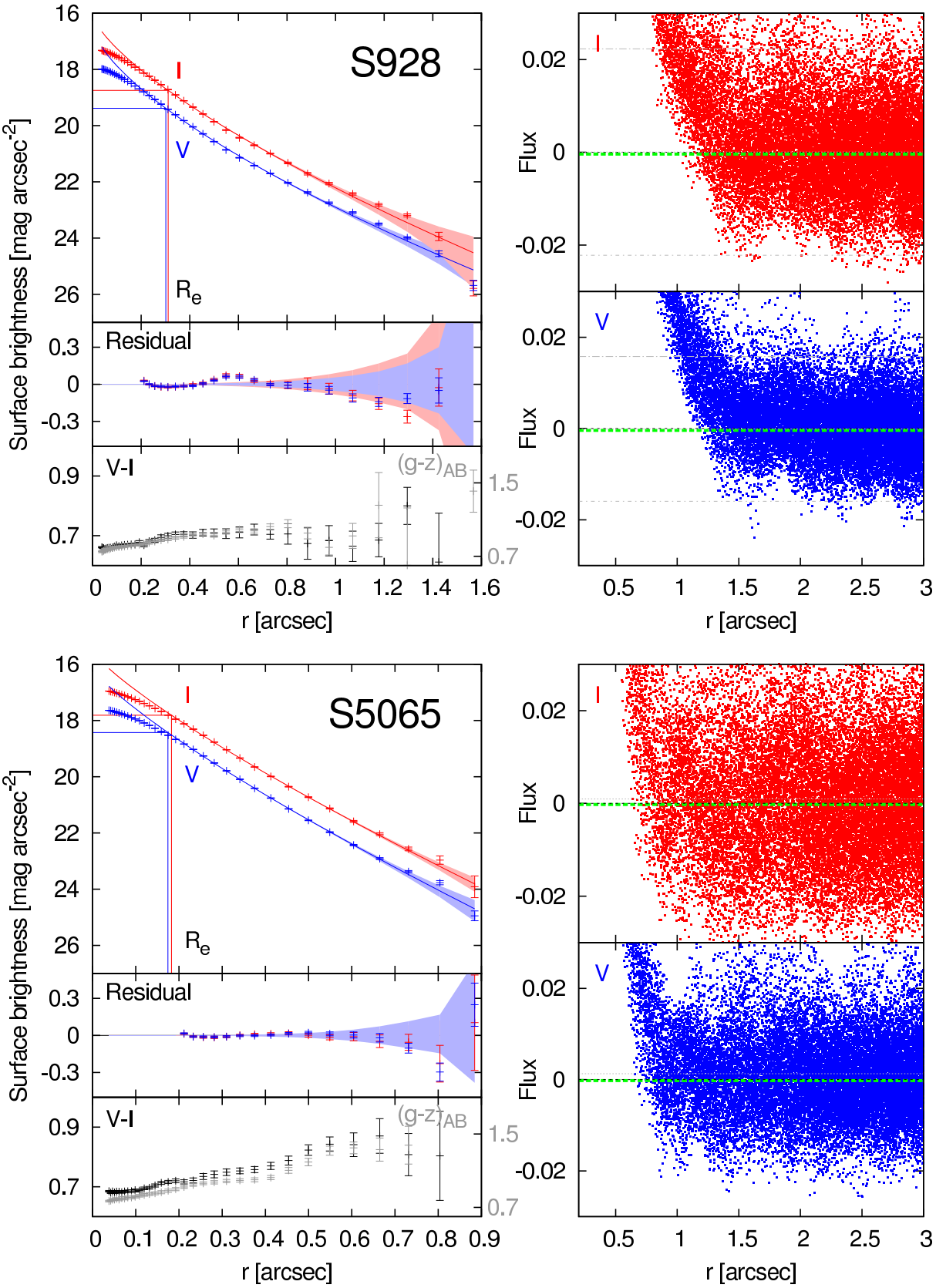

Figure A1 – *continued*